Journal of Power Sources 306 (2016) 248–257

Contents lists available at ScienceDirect

Journal of Power Sources

journal homepage: www.elsevier.com/locate/jpowsour

High energy asymmetric supercapacitor with 1D@2D structured $NiCo_2O_4$@Co_3O_4 and jackfruit derived high surface area porous carbon

Palanichamy Sennu [a], Vanchiappan Aravindan [b], Yun-Sung Lee [a, *]

[a] Faculty of Applied Chemical Engineering, Chonnam National University, Gwang-ju 500-757, Republic of Korea
[b] Energy Research Institute @ NTU (ERI@N), Nanyang Technological University, Research Techno Plaza, 50 Nanyang Drive 637553, Singapore

HIGHLIGHTS

- High surface area porous carbons are obtained from bio-mass waste Jackfruit peel.
- Pseudocapacitive 1D@2D structured $NiCo_2O_4$@Co_3O_4 is prepared by hydrothermal approach.
- Asymmetric supercapacitor (ASC) is assembled with aforesaid electrodes.
- ASC delivered the maximum energy density of 42.5 Wh kg^{-1} with good cycleability.

GRAPHICAL ABSTRACT

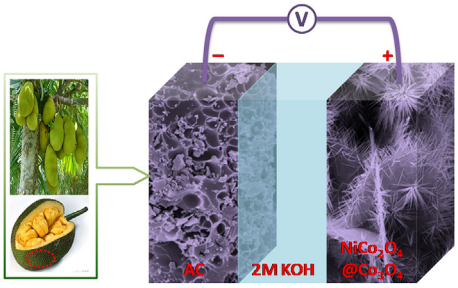

ARTICLE INFO

Article history:
Received 23 September 2015
Received in revised form
20 November 2015
Accepted 8 December 2015
Available online 17 December 2015

Keywords:
Asymmetric supercapacitor
Activated carbon
Jackfruit
Pseudocapacitance
Energy density

ABSTRACT

We report the fabrication of high energy asymmetric supercapacitor (ASC) using pseudocapacitive 3D microstructured composite $NiCo_2O_4$@Co_3O_4 and double layer forming activated carbon (AC). The pseudo capacitive electrode is synthesized *via* a facile two step hydrothermal process and AC is obtained from the bio-waste, Jackfruit (JF) peel by chemical activation. Extensive powder characterization and optimization has been conducted for both electrodes, especially in electrochemical aspect. The ASC is fabricated using JF derived AC as anode and $NiCo_2O_4$@Co_3O_4 cathode in aqueous media. Prior to the ASC assembly, the mass loading between the electrodes are adjusted based on the single electrode performance of both components *vs.* Ag/AgCl. The ASC is capable of delivering a maximum energy density of 42.5 Wh kg^{-1} at power density of 80 W kg^{-1}. In addition, the ASC rendered excellent cycleability, for example, the cell retains ~97% of initial capacitance after 7000 cycles. The outstanding performance of the ASC is originated from the well-developed building blocks of porous electrodes. An impedance study is also conducted to corroborate the excellent performance of $NiCo_2O_4$@Co_3O_4 *vs.* JF derived AC based ASC.

1. Introduction

Supercapacitors are considered as promising energy storage device for hybrid electric vehicles (HEV) and many industrial applications owing to its low cost, excellent round trip efficiency devices, long cycle life etc [1–5]. It is known fact that the performance and durability of supercapacitors are mainly depends on the choice of electrode and electrolytes used. In general, the supercapacitor means electric double layer capacitors (EDLC), and it is fabricated with high surface area carbons, preferably activated carbon (AC) in symmetric fashion in the presence of aqueous media

* Corresponding author.
E-mail address: leeys@chonnam.ac.kr (Y.-S. Lee).

http://dx.doi.org/10.1016/j.jpowsour.2015.12.029
0378-7753/

[4]. The high surface area involves the double layer formation by physical process (non-Faradaic) *i.e.* adsorption/desorption with solvated ions [6]. Though excellent power capability is noted for such supercapacitors, but the energy density remains an issue [7]. The discovery of fast faradaic reactions *i.e.* pseudocapacitive in transition mental oxides certainly leads to the possibility of widening energy density when coupled with carbonaceous electrode in asymmetric fashion. In this case, one electrode undergoes fast Faradaic reaction and other involves electric double layer formation in asymmetric fashion which in turn provides the higher energy density with extended working potential [2]. Similar to EDLC, the material choice and its morphology is crucial for pseudocapacitive components to yield the high energy density, since surface only undergoes the redox reactions. Thus, high surface area materials are preferred for the fabrication asymmetric supercapacitor (ASC) [1,8]. Nevertheless, similar concept has been successfully employed for the fabrication of Li-ion hybrid electrochemical capacitor (Li-HEC) in organic medium, and commercialized as well (ULTIMO) [6]. Unfortunately, the power capability of Li-HEC is not in the desired level for high power applications [9]. Therefore, development of high performance supercapacitors with high energy and power capabilities are desperately required. In this line, we report the fabrication of high energy ASC using AC from bio-waste, Jack fruit and $NiCo_2O_4$ nanorods grown over Co_3O_4 nanosheets (Co_3O_4-NS).

For EDLC component, high surface area carbon is preferred, since the capacitive behavior is completely depends on the formation of double layer across the electrode/electrolyte interface. High surface area with tailored meso/micro pores morphology determines the performance of the electrode [10,11]. Stable physiochemical properties of AC obtained from agricultural waste is considered to be a very important feedstock by considering two factors, they are easily available in a cost effective manner, and renewable as well. So far numerous bio-wastes such as fruit stones, seeds hulls (like, cottonseed, peanut), straw and stalks (corn, rice), wastes of wood industry and other low cost lignocelluloses materials have been explored as suitable precursor for the preparation of AC owing to its high carbon and low ash contents [3,7,11–15]. Amongst, jackfruit (*Artocarpus heterophyllus*) is one of the commonly used fruits in the world. The seeds are also used for cooking purpose. Moreover, there is no in-season or out-of-season for jackfruit. Therefore, it can be harvested round the year. Jackfruit peel/skin (JF) wastes have no economic value at all and it often creates a serious problem of disposal which creates local environmental issues. Conversion/recycling of JF into efficient AC would certainly increase the economic value. JF has high carbon content with heterogeneous porous microstructures and different functionalities. This certainly attributes to enable the JF derived AC to be used as high performance electrode for the fabrication supercapacitors.

Various simple transition metal oxides, such as RuO_2, MnO_2, $Ni(OH)_2$, NiO, Co_3O_4 etc. exhibits good pseudocapacitive nature in alkaline solutions [16–21]. Among them, Co-based ternary composites ($NiCo_2O_4$, $MnCo_2O_4$, etc.) are found appealing owing to the richness in redox reaction, an excellent electrical conductivity than binary oxides, low resistive ionic diffusion pathways, and high theoretical capacitance [22,23]. In this line, we have chosen Co_3O_4 and $NiCo_2O_4$ as pseudocapacitive components [24]. Though, numerous reports are available for the performance of both electrodes in alkaline media, but most of them in the single electrode configuration. However, few reports could be traced on the performance of such electrodes in a complete cell *i.e.* ASC [1,25–31]. In real time applications, a performance with counter electrode (preferably carbonaceous counterpart) is desperately required. Although, MnO_2/AC or conducting polymers based ASC is extensively reported in aqueous medium, but it displayed a inferior energy density only (<29 Wh kg^{-1}) [1,25]. Structural modification/designing is one of the efficient ways to achieve high energy density without compromising power capability and cycleability, since the redox reactions mainly occurred on the surface [32]. Hence, designing three-dimensional (3D) nanostructures with free voids based on low-dimensional (1D and/or 2D) building blocks are seems promising to fulfill the above requirements and challenging for supercapacitor point of view as well. First, we synthesized 2D Co_3O_4-NS *via* hydrothermal process [33] and flower like 1D $NiCo_2O_4$ nanorods were grown over above 2D nanosheets in the same approach. This two-step hydrothermal approach enables the synthesis of highly crystalline, 3D architectured $NiCo_2O_4$@Co_3O_4 composite.

In the present work, we have attempted to explore the possibility of constructing high performance ASC using these two fascinating electrodes in aqueous media (2 M KOH). An extensive electrochemical study includes the optimization of AC and $NiCo_2O_4$@Co_3O_4 in single electrode configuration and in complete ASC assembly as well. In addition, structure and composition of these materials were characterized and described in detail.

2. Experimental section

2.1. Preparation of AC and $NiCo_2O_4$@Co_3O_4

Artocarpus heterophyllus skin (JF) was used as the starting material for the preparation of AC. First, the waste wet skin were washed with water for several times and cut into small pieces. The small pieces were charred at 150 °C for 1 h. Then the black colour char was ground into fine powder and treated with 1:2 weigh ratio of KOH at 120 °C for 3 h. Then, the mixture was activated at 800 and 900 °C under N_2 flow at heating rate of 5 °C $min.^{-1}$ for 3 h. After cooling down to room temperature, the resultant product was washed thoroughly with de-ionized water for several times until the pH value became neutral. The washed powder was vacuum dried and subsequently used for various characterization studies. JF derived AC obtained at 800 °C with KOH weight ratios of 1:0 and 1:2 were designated as JF-1 and JF-2, respectively. JF-3 was obtained from the activation conducted at 900 °C for 1:2 ratios of KOH.

The 1D $NiCo_2O_4$ nanorods over 2D Co_3O_4-NS was synthesized by two-step hydrothermal method. In a typical process, stoichiometric amounts of $Ni(NO_3)_2 \cdot H_2O$ (Junsei, Japan), $Co(NO_3)_2 \cdot H_2O$ (Junsei, Japan) and urea were dissolved in 25 ml of water. After stirring for 20 min, appropriate amount of Co_3O_4-NS (200 mg) was added into the above greenish-pink solution. Then, the mixture was transferred in to 50 ml of Teflon lined autoclave and treated at 160 °C for 2 h. After cooling down to room temperature, the intermediate product was harvested and washed with water and ethanol repeatedly, and dried at 60 °C for overnight. Finally, the resultant product was calcined at 300 °C for 4 h in air to yield such fascinating $NiCo_2O_4$@Co_3O_4 composite. The detailed procedure for synthesis of 2D Co_3O_4-NS was reported by us in the previous works [33,34].

2.2. Physical characterization

Crystalline phase of the resultant materials were studied by powder X-ray diffraction (XRD, Rint 1000, Rigaku, Japan) using CuKα radiation. BET surface area measurements were performed by using a Micromeritics ASAP 2010 surface area analyzer. Morphological features of the samples were recorded using field emission scanning electron microscope (FE-SEM, S4700, Hitachi, Japan). X-ray photoelectron spectroscopy (XPS) was performed using

Multilab 2000, UK with monochromater Al Kα radiation ($h\nu = 1486.6$ eV).

2.3. Electrochemical characterization

Composite electrodes were formulated with accurately weighed amounts of active materials (JF-1, JF-2, JF-3 and $NiCo_2O_4$@Co_3O_4, 80% or 5 mg), ketzen black (10%), and teflonized acetylene black (10%, TAB-2) using ethanol. The resultant slurry was pressed over nickel foam and dried at 160 °C for 4 h in a vacuum oven. A typical single/three-electrode glass cell equipped with a working electrode, stainless steel mesh (counter electrode), and Ag/AgCl as a reference electrode were used for electrochemical measurements. ASC was constructed in two-electrode coin-cell (CR 2032) configuration separated by a Hyundai filter paper (micro-90 mm) and filled with electrolyte solution. 2 M KOH was used as the electrolyte for both single electrode and ASC assemblies. Electrochemical measurements like cyclic voltammetry (CV) and electrochemical impedance spectroscopy (EIS) were recorded using an electrochemical work station (Bio-Logic, SP-150, France). Galvanostatic charge–discharge and cycle stabilities were studied by conventional battery tester (WBCS 3000, Won-A-Tech, Korea) at ambient conditions. The electrochemical parameters such as specific capacitance, average internal resistance, coulombic efficiency, and energy & power densities of the ASC were calculated by using formulas described elsewhere [35].

The corresponding specific capacitance was calculated from the following equations:

$$C = \frac{I \times \Delta t}{m \times \Delta V}$$

where C_m is the specific capacitance (F g^{-1}), I is applied current (A), Δt represents discharge time (s), ΔV represents the potential window (V) and m is the total mass of the ASC (g).

$$E = 0.5C(V)^2$$

$$P = \frac{E}{t}$$

where E (Wh kg^{-1}) is the energy density and P (W kg^{-1}) is the power density.

3. Results and discussion

XRD analysis was performed to examine the crystal structures of the as-prepared $NiCo_2O_4$@Co_3O_4 nanostructures and JF derived AC (Fig. 1). The observed XRD pattern of $NiCo_2O_4$@Co_3O_4 is compared with the standard reflections of individual $NiCo_2O_4$ (ICDD no. 01-073-1702) and Co_3O_4 (ICDD no. 01-076-1802) phases [24]. Further, the XRD pattern of 2D structured Co_3O_4-NS also given for comparison. It can be seen that the $NiCo_2O_4$ crystal orientations are perfectly matched with Co_3O_4 pattern which is indicate the formation of phase pure cubic spinel structure. Further, there are no additional peaks observed upon the hydrothermal process during $NiCo_2O_4$ nanorods growth and subsequent calcination. This clearly suggests that the crystal structure of Co_3O_4-NS is not influenced upon hybridization with 1D $NiCo_2O_4$ nanorods. On the other hand, in AC, the XRD pattern showed the absence of sharp and strong reflections for JF derived carbons which clearly suggest the presence of randomly oriented amorphous phase [36]. The rise inactivation temperature (800–900 °C) leads to removal of the loosely bounded amorphous carbon by de-gassing them as CO, and increase in the degree of graphitization (JF-3) during activation process. This has been clearly evident from the variation of peak (100) intensity at ~43° compared to JF-2 [37].

The porous nature of $NiCo_2O_4$@Co_3O_4 and JF derived AC were

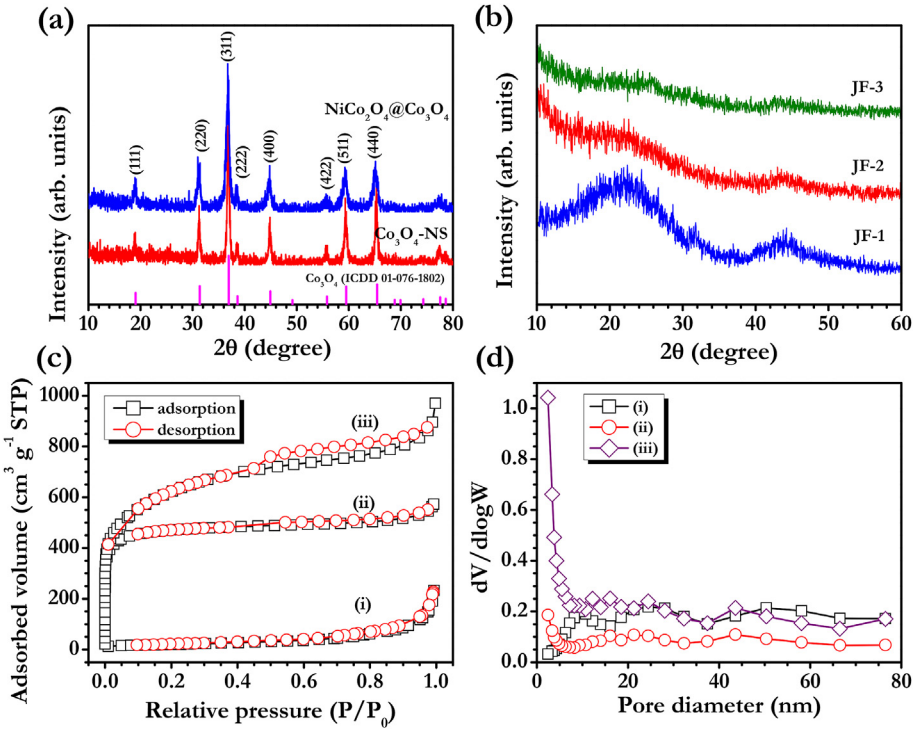

Fig. 1. (a) XRD pattern of $NiCo_2O_4$@Co_3O_4 and Co_3O_4-NS, (b) XRD pattern of activated carbons derived from *Artocarpus heterophyllus*, (c) N_2 adsorption/desorption isotherms of (i) $NiCo_2O_4$@Co_3O_4, (ii) JF-2 and (iii) JF-3, and (d) pore size distribution of (i) $NiCo_2O_4$@Co_3O_4, (ii) JF-2 and (iii) JF-3.

Table 1
BET surface area, total pore volume and Average pore diameter of different *Artocarpus heterophyllus* derived AC (JF-1, JF-2 & JF-3), $NiCo_2O_4$@Co_3O_4 and Co_3O_4-NS.

Sample	SBET[a] ($m^2\ g^{-1}$)	V_{total}[b] ($cm^3\ g^{-1}$)	V_{micro}[c] ($cm^3\ g^{-1}$)	V_{meso}[d] ($cm^3\ g^{-1}$)	Average pore diameter (nm)
JF-1	128	0.63	–	–	1.97
JF-2	1794	0.88	0.71	0.16	1.96
JF-3	2235	1.41	0.99	0.41	2.52
$NiCo_2O_4$@Co_3O_4	73.43	0.32	–	–	17.58
Co_3O_4-NS	27.15	0.16	–	–	22.36

[a] S_{BET} is the BET surface area.
[b] Total pore volume (V_{total}) was the single point adsorption total pore volume of pores less than 400 nm diameter at $P/P_0 = 0.990$.
[c] V_{micro} is the micro pore volume.
[d] V_{meso} is the meso pore volume.

analyzed by N_2 adsorption–desorption isotherms and given in Fig. 1c. As shown in Fig. 1c, the major uptake of N_2 occurs relatively at low pressure (<0.1) for JF derived AC (JF-1 and JF-2), which is a fingerprint of type-I isotherm with microporous structure. In the case of JF-3, a steep increase in the amount of N_2 adsorption was evident and a distinct hysteresis loop can be observed in the P/P_0 range of 0.7–0.99. This suggest that the increases of temperature creates a mixed type I and type IV isotherms, and the hysteresis loop at high relative pressures (P/P_0) indicates the existence of both micro-and meso-porous structure [10,15]. In the case of NiC-o_2O_4@Co_3O_4, the amount of N_2 adsorptions at high pressure >0.8 indicates the presence of mesoporous structure only [11]. Fig. 1d illustrates the BJH pore size distributions of both $NiCo_2O_4$@Co_3O_4 and JF derived AC. BET specific surface area and pore size distributions were calculated for all the materials and given in Table 1. It is evident that BET specific surface area increases with rise in temperature, especially for JF-3. For example, specific surface area and total pore volumes are found to be 2235 $m^2\ g^{-1}$ and 1.4057 $cm^3\ g^{-1}$, respectively for JF-3. Such an ultra-high specific surface area with porous architecture certainly makes the JF derived AC to be used as attractive material for supercapacitor applications.

Morphology and microstructure of the $NiCo_2O_4$@Co_3O_4 and JF derived AC (JF-2 and JF-3) were analyzed by FE-SEM and given in Fig. 2. Fig. 2a exhibits the presence of sponge-like irregular granules with three-dimensional porous network and observed in micrometer-level for JF-2. This irregular surface leads to increasing the contact area, which facilitates the ions diffusion for double layer formation across the electrode/electrolyte interface. At higher temperature (900 °C), the portion of amorphous carbon has been transformed in to the ordered flake-like morphology. Further, the granules are not completely exfoliated, which is clearly seen from the appearance of arrays of relatively thick layer [38] (Fig. 2b-inset). Apparently, finer granularity and well-developed microstructure could favorable for fast charge-transfer and enhanced charge storage capacity. Fig. 2c shows the FE-SEM images of $NiCo_2O_4$@Co_3O_4 with rod-like $NiCo_2O_4$ microstructure are grown over all surfaces of Co_3O_4-NS. Morphological features of the 2D structured Co_3O_4-NS is given in Fig. S1 and reported by us elsewhere [33]. The bunch of rods is grown upwards by vertically and inclined positions from the surface (Fig. S2). The length of nanorods is between 0.7 and 1.5 μm and clearly shown in Fig. 2d. Further, this structure composed of regular nanoflowers with open-up network structure. Most of the $NiCo_2O_4$ nanorods would forms a bundle like packed structure with Co_3O_4-NS and formatting of the 3D architecture.

Surface chemical composition *i.e.* functional groups of the JF derived AC is selectively studied (JF-2) by employing XPS along with $NiCo_2O_4$@Co_3O_4 nanostructures and given in Fig. 3. The survey

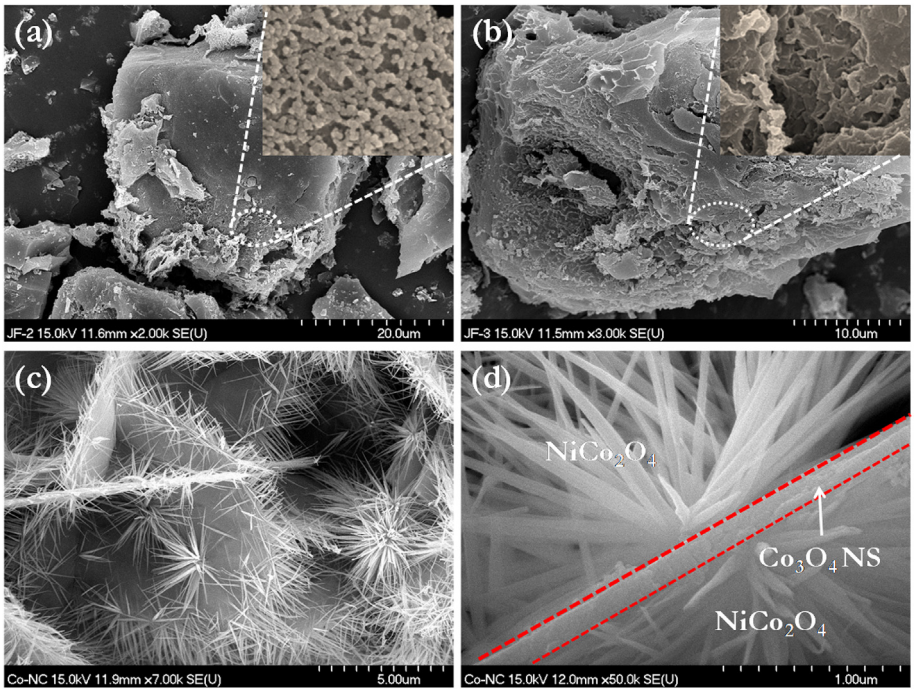

Fig. 2. FE-SEM images of *Artocarpus heterophyllus* derived activated carbons (a) JF-2 and (b) JF-3, (c–d) the 1D $NiCo_2O_4$ nanorods grown over and below the Co_3O_4 nanosheets with lower and higher magnifications.

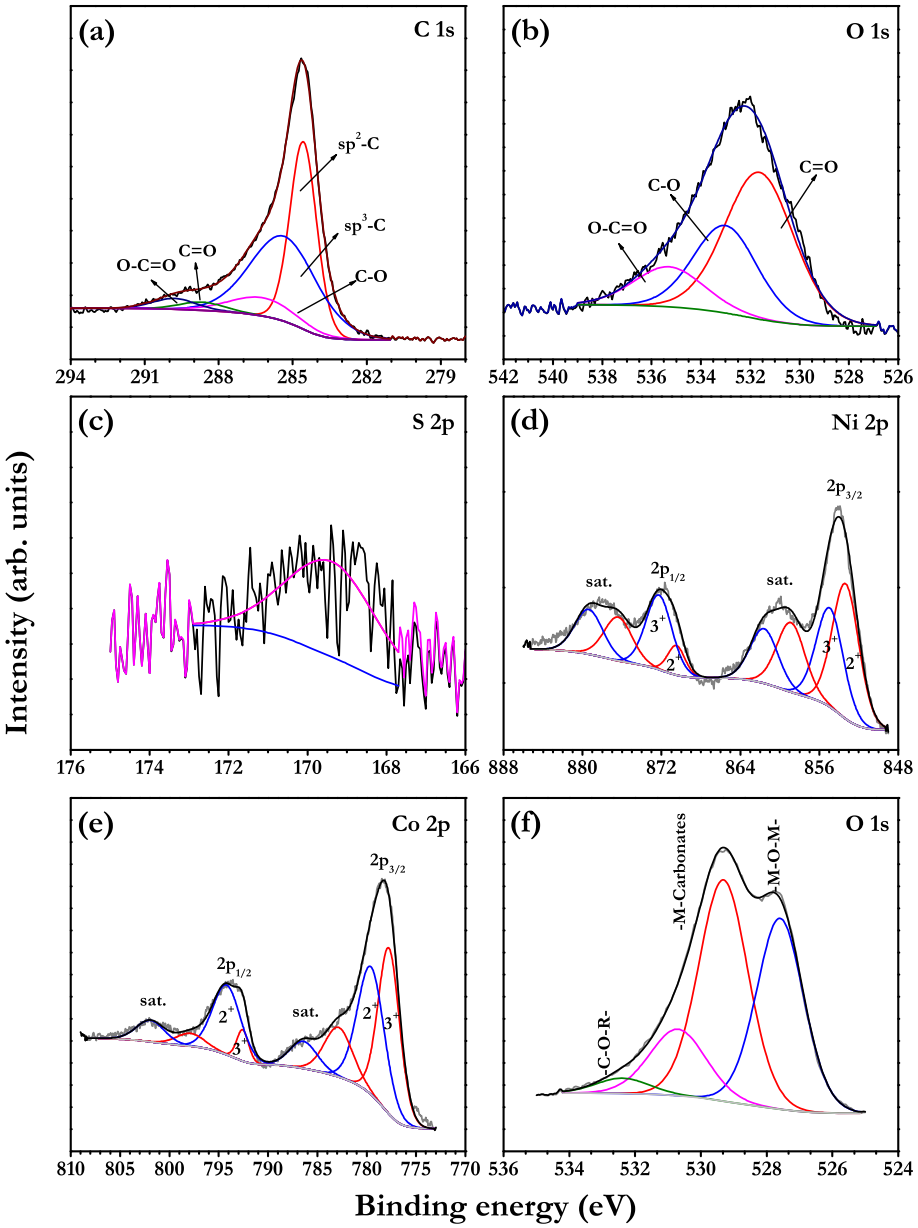

Fig. 3. XPS spectrum of *Artocarpus heterophyllus derived activated* carbons. Core level spectra of (a) C 1s, (b) O 1s, (c) S 2p, and Core level spectra of (d) Ni 2p, (e) Co 2p and (f) O 1s from $NiCo_2O_4$@Co_3O_4.

spectrum of JF-2 sample consists of different elements like O and S, apart from C (Fig. S3) [39,40]. In JF-2, the atomic percentage of C, O and S is found to be 74, 25.5 and 0.85%, respectively. By using a Gaussian fitting method, in core level C 1s spectra, (Fig. 3a) most pronounced peak at 284.6 eV is a characteristic of C═C, and rest of the peaks are corresponds to C–S, C–O and C═O in sequence [41]. Further de-convolution of O 1s spectrum for identification of surface functionalities are shown in Fig. 3b. The spectra was obtained by fitting three component peaks, which are attributed to C═O (531.6 eV), C–O (533 eV) and O–C═O (535.3 eV), respectively [42,43]. The high-resolution S 2p spectrum in Fig. 3c clearly reveals the presence of C–S–O (169.4 eV) bonds. The existence of such surface functionalities is very important for the application of supercapacitors, since it not only improves the wettability, but also facilitates fast redox reactions in alkaline medium [44]. As a result, rise in pseudocapacitive behavior is noted. The survey spectrum of $NiCo_2O_4$@Co_3O_4 composed of Ni, Co and O elements, whereas Co_3O_4-NS contains only Co and O (Fig. S3). The de-convolution of Co 2p peaks shows two spin–orbit doublets separated by 15 eV which is a characteristic of $Co^{3+}$and Co^{2+} ions. The Ni 2p is also fitted with two spin–orbit doublets and shakeup satellites are associated with characteristic Ni^{2+} and Ni^{3+} ions [40]. The O 1s shows a large M–O–M peak at 527.6 eV which is an indicative of most of the oxygen in the lattice and other three peaks at 529.26, 532.83 and 531.15 eV, are associated to the M = O, M-C═O and O–C═O bonds, respectively. The binding energies of these peaks are consistent with the literature and signify the formation of $NiCo_2O_4$ [39].

4. Electrochemical studies

4.1. Single electrode performance of JF derived AC (JF-2 and JF-3)

Carbon is one of the unique and fascinating material used in supercapacitor applications, and it can be used as positive, or

negative electrodes irrespective of the configuration (symmetric, asymmetric or hybrid configuration) and electrolytes (aqueous or organic) [4,36,45]. In the present work, an attempt has been made to exploit the possibility of using JF derived AC as negative electrode for charge storage. First, supercapacitive behavior was estimated through single electrode configuration and eventually paired with $NiCo_2O_4$@Co_3O_4 nanostructures in asymmetric fashion under the optimized loadings. In a symmetric configuration, the applied potential is equally divided by both electrodes, whereas in ASC, the potential is divided by based on the specific capacitance of the individual electrodes [10,46]. Hence, single/three electrode performance is desperately required and crucial for the optimization. The electrochemical and capacitive properties of the JF derived AC were evaluated using three-electrode geometry with 2 M KOH as electrolyte and Ag/AgCl as reference electrode. First, the optimization of potential window was performed using tentatively for JF-2 at a scan rate of 5 mV s^{-1} and given in Fig. 4a. The lower cut-off potential is varied from −0.8 to −1.2 V *vs.* Ag/AgCl with respect to 0 V *vs.* Ag/

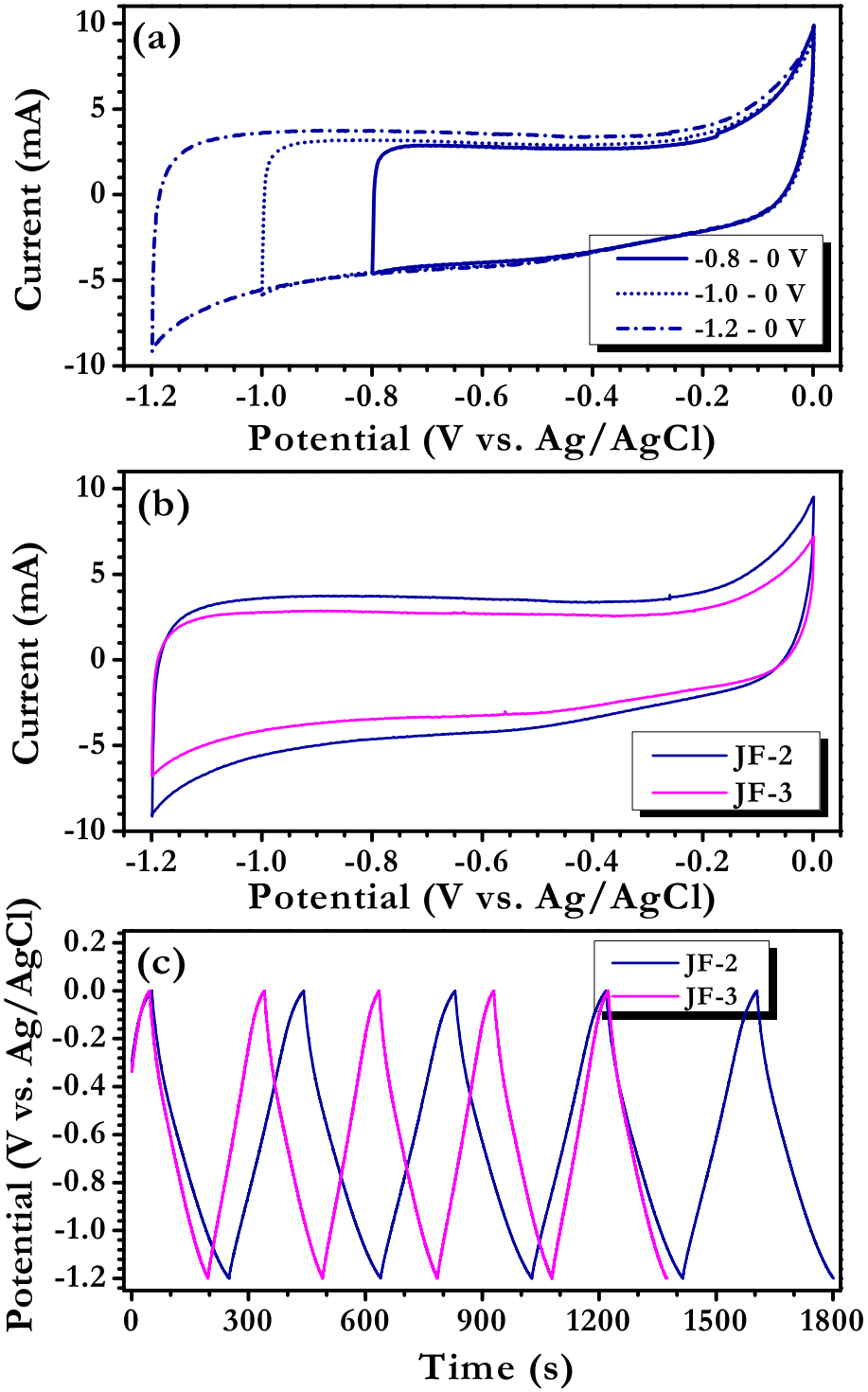

Fig. 4. Electrochemical performance of JF derived AC *vs.* Ag/AgCl in 2 M KOH solution. (a) CV curves of JF-2 in different voltage window at 5 mV s^{-1}, (b) CV curves at 5 mV s^{-1}, and (c) galvanostatic charge–discharge curves at current density of 1 A g^{-1}.

AgCl. The JF-2 showed excellent capacitive behavior irrespective of the potential windows with close to ideal rectangular shaped CV traces [38]. This is an indicative of irreversible reaction occurred when potential is lower than −1.2 V *vs.* Ag/AgCl. Hence, we have fixed −1.2 to 0 V *vs.* Ag/AgCl range for further investigation. Next, we compared the electrochemical performance of both JF-2 and JF-3 in the same scan rate and the observed results are given in Fig. 4b. Reduction of ~0.6% active capacitive area is noted for JF-3 compared to JF-2. This confirms the inferior electrochemical activity of JF-3. Galvanostatic charge–discharge studies are also conducted for JF derived AC (JF-2 and JF-3) to ensure the CV analysis and shown in Fig. 4c. Both JF-2 and JF-3 exhibits the ideal triangular shaped charge–discharge curves *i.e.* linear variation of potential with respect to time (a typical capacitance behavior of carbonaceous materials *via* electric double layer formation). The specific capacitance of JF-2 and JF-3 are calculated to 375 and 295 F g^{-1}, respectively. We strongly believe that the enhanced double layer capacitance is resulted from the presence of micro pores with an extended surface functionalities in JF-2 compared to JF-3. Also the contribution from the presence of surface functional groups cannot be excluded. Therefore, we have chosen JF-2 for further studies and to be used as promising negative electrode for the fabrication of ASC. Nevertheless, JF-3 is also subjected for CV and galvanostatic measurements at various conditions and given in Fig. S4. Fig. 5a shows the family of CV traces recorded in a single electrode configuration at various scan rates. The JF-2 AC demonstrated near ideal rectangular shaped signatures without any significant distortion while increasing the scan rate. More specifically, at higher scan rate (100 mV s^{-1}), more or less rectangular shape is preserved which indicates the facile ion transportation and excellent high power capability. Fig. 5b represents the galvanostatic charge–discharge curves of JF-2 at various current densities. As expected, specific capacitance is decreased with the faster current loads, for instance, JF-2 delivered specific capacitance of 375 F g^{-1} at current density of 1 A g^{-1}, while the current density is increased to 8 A g^{-1}, the specific capacitance of 280 F g^{-1} only observed. The observed specific capacitance values are better than other bio-mass precursor used for the preparation of high surface area carbons reported elsewhere [7,12].

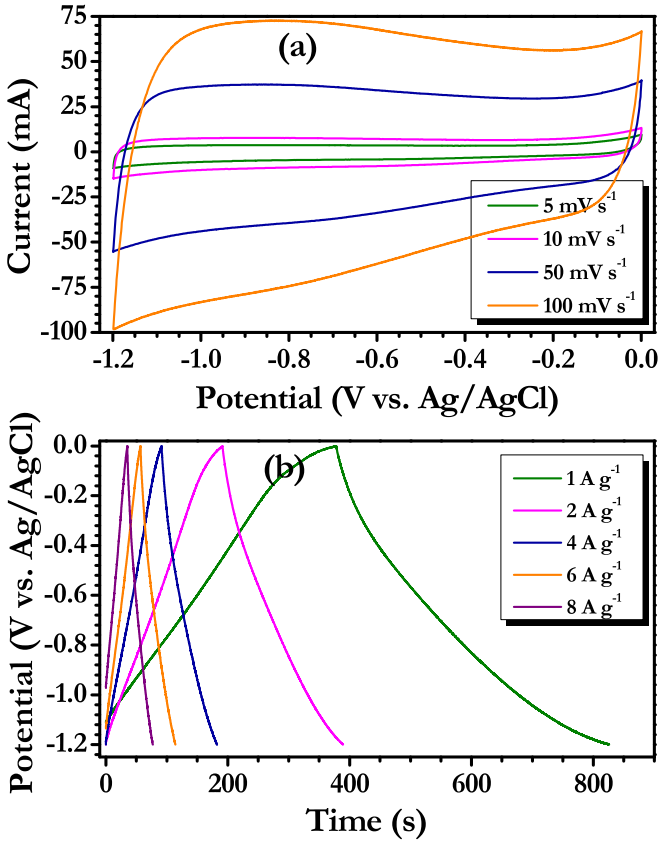

Fig. 5. Electrochemical performance of JF-2 *vs.* Ag/AgCl in 2 M KOH solution, (a) CV curves recorded at different scan rates between 0 to -−1.2 V *vs.* Ag/AgCl, (b) galvanostatic charge–discharge curves at different current densities.

4.2. Single electrode performance of $NiCo_2O_4$@Co_3O_4

To validate the advantages of hierarchical growth 1D $NiCo_2O_4$ nanorods over Co_3O_4-NS, we investigated the electrochemical performance of $NiCo_2O_4$@Co_3O_4 and Co_3O_4-NS in single electrode configuration with 2 M KOH solution. First, the optimization of potential window was performed at scan rate of 5 mV s^{-1} for $NiCo_2O_4$@Co_3O_4 nanostructures (Fig. S5a). Apparent to note that the increase in the potential beyond 0.4 V *vs.* Ag/AgCl is certainly leads to serious limitations of the cell owing to the O_2 evolution reaction at the electrode. Hence, the electrochemical performance of pseudocapacitive $NiCo_2O_4$@Co_3O_4 electrode is limited to 0–0.4 V *vs.* Ag/AgCl region [47]. Also the electrochemical activity of Co_3O_4-NS was conducted in the same region for comparison purpose and given in Fig. 6a. It can be seen from the CV curves, $NiCo_2O_4$@Co_3O_4 nanostructures exhibits more distinct peaks and large area underneath the curve than Co_3O_4-NS. This clearly reflecting the electrochemical process between these two samples is quite different and the $NiCo_2O_4$@Co_3O_4 delivered a higher specific capacitance than Co_3O_4-NS. The following equilibrium describes the overall electrochemical activity of $NiCo_2O_4$@Co_3O_4 and Co_3O_4-NS in aqueous media,

$$NiCo_2O_4 + OH^- + H_2O \leftrightarrow NiOOH + 2CoOOH + e^-$$

$$2CoOOH + OH^- \leftrightarrow 2CoO_2 + H_2O + e^-$$

$$Co_3O_4 + OH^- + H_2O \leftrightarrow 3CoOOH + e^-$$

$$CoOOH + OH^- \leftrightarrow CoO_2 + H_2O + e^-$$

As the scan rate is increased from 5 to 50 mV s^{-1}, the linear variation of peak currents with applied potentials was observed (Fig 6b). This is clearly suggest that the building blocks of hierarchical $NiCo_2O_4$ nanorods can certainly enhances, the electron transport to the Co_3O_4-NS owing to the 1D morphology and excellent electrical conductivity [24]. This implies that the electrode kinetics is controlled by diffusion of ions with fast interfacial Faradaic reactions [1]. In contrast, the as-prepared Co_3O_4-NS showed a sluggish kinetics with marginal current response compared to the $NiCo_2O_4$ nanorods, which is clearly observed from CV studies [27]. This is a good agreement with the results obtained from galvanostatic charge–discharge measurement for Co_3O_4-NS (Fig. S5b & c). The $NiCo_2O_4$@Co_3O_4 delivered the specific capacitances of 430 and 420 F g^{-1} at current density of 1 and 8 A g^{-1}, respectively (Fig. 6c). This clearly showed 97.6% of initial capacitance is retained, even at high current testing conditions. A small capacitance contribution from the Co_3O_4-NS cannot be ignored for such performance. On the other hand, Co_3O_4-NS displayed a maximum specific capacitance of 113 F g^{-1} at low current rates (1 A g^{-1}). The observed results are comparable to the results reported on $NiCo_2O_4$ based composites [24].

Fig. 6d shows the combined plot of specific capacitances with respect to applied currents for JF-2, JF-3, Co_3O_4-NS and $NiCo_2O_4$@Co_3O_4 in a single/three electrode configuration *vs.* Ag/AgCl electrode. As mentioned above, $NiCo_2O_4$@Co_3O_4 (430 F g^{-1}) and JF-

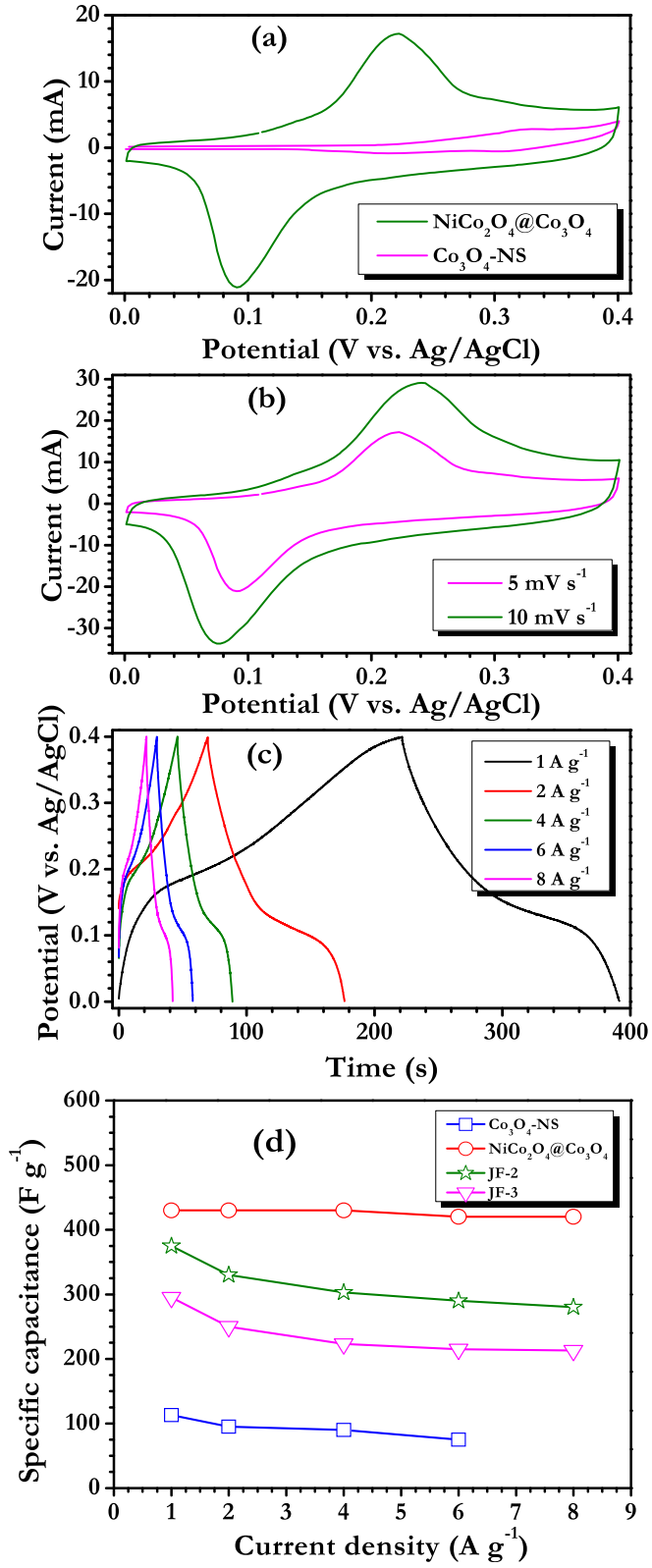

Fig. 6. (a) Comparison of CV curves for $NiCo_2O_4@Co_3O_4$ and Co_3O_4-NS *vs.* Ag/AgCl in 2 M KOH solutions at scan rate of 5 mV s^{-1}, (b) CV traces of $NiCo_2O_4@Co_3O_4$ at different scan rates, (c) galvanostatic charge–discharge curves of $NiCo_2O_4@Co_3O_4$ at different current densities, (d) Specific discharge capacitance of $NiCo_2O_4@Co_3O_4$, Co_3O_4-NS, JF-2 and JF-3 in single electrode configuration *vs.* Ag/AgCl in 2 M KOH solution at various current rates.

2 (375 F g^{-1}) are displayed the highest specific capacitances for positive and negative electrode evaluations at current density of 1 A g^{-1}, respectively. The observed values are much higher than other candidates are tested under the similar circumstances, likely Co_3O_4-NS (113 F g^{-1}) and JF-3 (295 F g^{-1}). Just testing the electrode materials in single/three electrode configuration is not useful for end user applications. Hence, ASC is fabricated by adjusting the mass loading between the electrodes to realize the high energy density. The detailed information about the ASC fabrication and its electrochemical performances are discussed in the forthcoming sections.

4.3. Fabrication of asymmetric supercapacitor (ASC) and its performance

ASC was fabricated in the presence of 2 M KOH electrolyte solution with $NiCo_2O_4@Co_3O_4$ and JF-2 as positive and negative electrode, respectively. Accordingly, the active mass of both positive and negative electrodes are balanced based on the charges stored in each electrodes, the adjusted mass ratio to be mJF-2/$m$$NiCo_2O_4@Co_3O_4$ = 0.87. ASC has been fabricated by keeping the aforesaid mass loadings and electrochemical performances are given Fig. 7. Fig. 7a shows the CV curves of ASC recorded at scan rate of 0.1 mV s^{-1} and performance of $NiCo_2O_4@Co_3O_4$ and JF-2 in a three electrode configuration also given for comparison. Similar to the single electrode performance, optimization of working potential is needed. Accordingly, the CV has been recorded at the scan rate of 5 mV s^{-1} for different upper cut-off potentials and given in Fig. 7b. Unlike the sharp redox peaks observed for $NiCo_2O_4@Co_3O_4$ in the single electrode studies, the ASC cell showed quasi-rectangular shaped curves even at the potential ranges from 1.4 to 1.6 V [42]. A mild decomposition of the electrolyte solution is observed at ~1.6 V. Hence, we stopped extending the potential window for optimization and fixed this region for further studies. Fig. 7c represents the family of CV signatures of ASC and examined between 0 and 1.6 V at various sweep rates (5–100 mV s^{-1}). When the sweep rate increased, shape of the CV curves remains unchanged which clearly suggests greater diffusion of electrons and ions to the inner regions of the electrode. As a result, fast electron/ion transport property is observed and it is one of the pre-requisite for high power electrochemical energy storage devices.

Fig. 8a and (Fig. S6) shows the typical charge–discharge curves of ASC at various current densities ranging from 0.1 to 4 A g^{-1}. The specific capacitances values are calculated from the discharge time, for instance, 119, 85 and 80 F g^{-1} is noted for the current densities of 0.1, 1 and 4 A g^{-1}, respectively. The charge–discharge pattern was symmetrical which indicates the excellent reversibility of electrodes with low polarization. The specific capacitance is decreased with an increase in current rate because of an increased ohmic drop and scarcity of active material at the electrode/electrolyte interface available for Faradaic and non-Faradaic reactions upon cycling. Cycleability is one of the important criterions to be employed in practical configuration [1,4]. Hence, cycling stability of the ASC was performed at a current density of 2 A g^{-1} and shown in Fig. 8b. It is evident that the capacitance of ASC increases ~12% after 1000 cycles, suggesting the improvement in surface wetting, pore accessibility to electrolyte ions and activation of the electrodes by the electrolytes upon repeated cycling [27,39,42]. Upon extended cycling, the specific capacitance remains as 97% after 7000 cycles, which is comparable to that of the previous reports [29–31,48]. Obviously, this is one of the good performances reported in the ASC configuration. Electrochemical impedance spectroscopy (EIS) is one of the important tools to understand the reactivity of the ASC. Hence, $NiCo_2O_4@Co_3O_4$ *vs.* JF-2 based ASC is subjected to EIS studies in the frequency range of 100 kHz to 0.02 Hz and given in Fig. 8c.

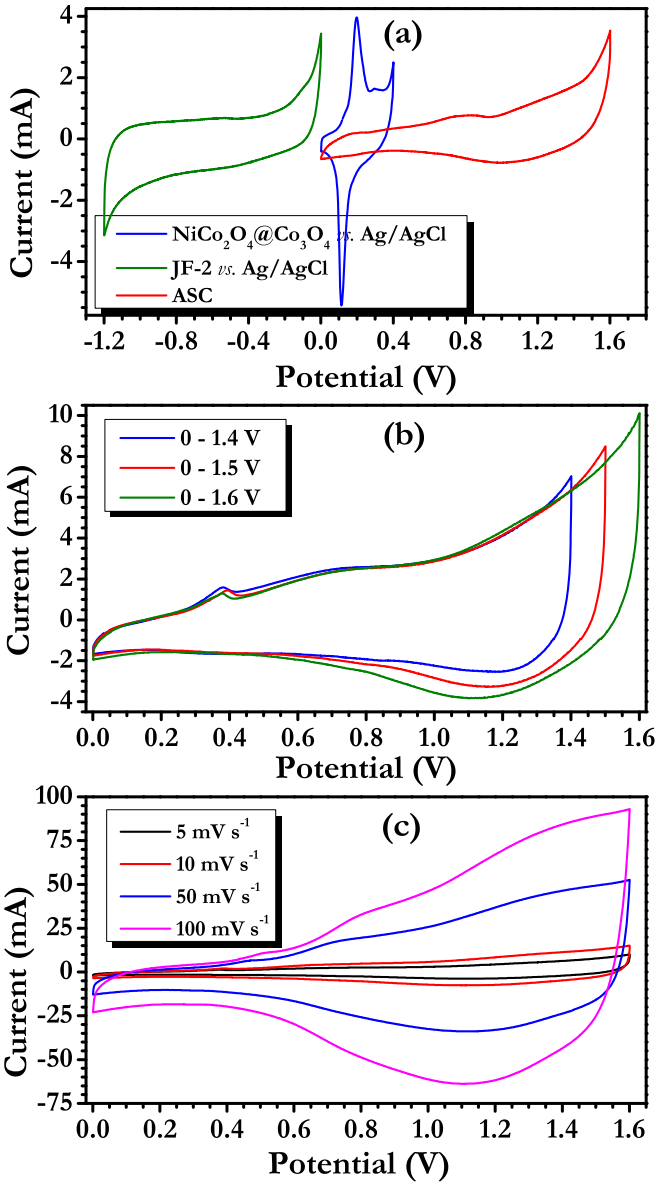

Fig. 7. (a) CV traces of $NiCo_2O_4@Co_3O_4$ and JF-2 in single electrode configuration *vs.* Ag/AgCl electrode, and ASC ($NiCo_2O_4@Co_3O_4$ *vs.* JF-2) in 2 M KOH solution at scan rate of 0.1 mV s^{-1} (b) CV curves of ASC in various potential windows at scan rate of 5 mV s^{-1}, and (c) comparison of CV curves for ASC at different scan rates.

The Nyquist plot of ASC was recorded before and after 7000 cycles. The magnitudes of solution resistance (Rs) in impedance response obtained for the ASC before and after 7000 cycles are found to be 0.192 and 0.436 Ω, respectively. This clearly showed that $NiCo_2O_4@Co_3O_4$ *vs.* JF-2 based ASC have negligible amount of side reaction with the electrolyte counterpart. This negligible variation validates the excellent stability of ASC upon long term cycling.

Energy and power densities of the $NiCo_2O_4@Co_3O_4$ *vs.* JF-2 based ASC were calculated according to the equation described above and shown in Fig. 8d. In addition, literature values of Ni-based ternary oxides are also given for comparison. Here, total mass of the active material (JF-2 + $NiCo_2O_4@Co_3O_4$) and discharge time were considered for the calculation of energy and power densities. The ASC delivered a maximum energy density of 42.5 Wh kg^{-1} at power density of 80 W kg^{-1}. As mentioned above, this is one of the best values reported for the ASC configuration irrespective of the

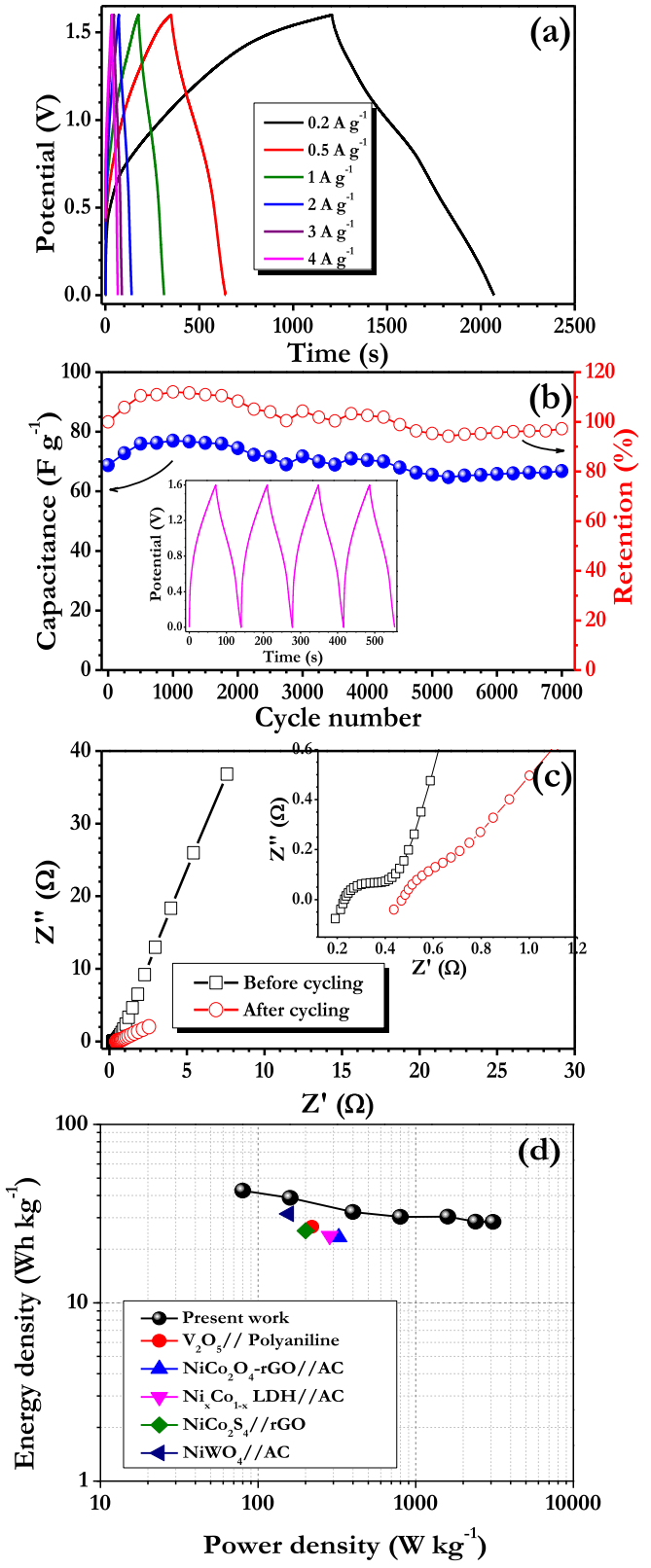

Fig. 8. (a) Galvanostatic charge–discharge of ASC at different current densities, (b) Cycling profiles of ASC at current density of 2 A g^{-1}, Inset: typical charge–discharge curves and (c) Nyquist plot of ASC recorded before and after cycling, Inset: magnified view, (d) Ragone plot of $NiCo_2O_4@Co_3O_4$ *vs.* JF-2 based ASC with previously reported ASC. AC: activated carbon, LDH: layered double hydroxide, rGO: reduced graphene oxide.

positive or negative electrodes, for instance, $NiCo_2O_4$@MnO_2//AC (35 Wh kg^{-1}) [27], $NiCo_2O_4$-rGO//AC (23.32 Wh kg^{-1}) [28], Ni_xCo_{1-x} layered double hydroxides//AC (23.7 Wh kg^{-1}) [29], $NiCo_2S_4$//rGO (31.5 Wh kg^{-1}) [30], $NiWO_4$//AC (25.3 Wh kg^{-1}) [31], and V_2O_5// Polyaniline (26.7 Wh kg^{-1}) [8] and various biomass high surface area carbons as well (Table S1). We strongly believe that, the combined features of JF derived AC and pseudocapacitive 1D structure grown over 2D sheets certainly leads to the excellent performance in asymmetric fashion. This approach can be easily extended to other materials for further exploration and unveiling new configurations with improved energy and power capability.

5. Conclusion

We successfully demonstrated the fabrication of high energy ASC using pseudocapacitive $NiCo_2O_4$@Co_3O_4 and double layer forming JF derived AC in alkaline media. The ASC delivered the high specific capacitance and energy density of 119 F g^{-1} and 42.5 Wh kg^{-1}, respectively. Also, excellent cycleability and capacitance retention characteristics were noted, for instance the ASC rendered ~97% of initial value after 7000 cycles. First, AC was derived from renewable bio-source waste, Jackfruit *via* chemical activation and 3D hybrid nanostructure of $NiCo_2O_4$@Co_3O_4 was constructed from flower like of 1D $NiCo_2O_4$ nanorods over 2D Co_3O_4 NS *via* two step hydrothermal processes. We strongly believe that the utilization of bio-waste from sustainable resources provided by nature and opening up a great potential application in high-performance energy storage systems. The concept of hybridizing 3D architecture electrode with AC from bio-mass certainly paved the new way for the construction of high performance electrochemical energy storage devices in a cost effective manner. This approach can also be extended for various bio-mass precursors and metal oxides with various nano-architectures for further exploration.

Acknowledgements

This work was supported by the National Research Foundation of Korea Grant funded by the Korean Government (MEST) (NRF-2011-C1AAA0010030538).

Appendix A. Supplementary data

Supplementary data related to this article can be found at http://dx.doi.org/10.1016/j.jpowsour.2015.12.029.

References

[1] T. Brousse, D. Bélanger, D. Guay, Asymmetric and hybrid devices in aqueous electrolytes, in: Supercapacitors, Wiley-VCH Verlag GmbH & Co. KGaA, Weinheim, Germany, 2013, pp. 257–288.
[2] E. Frackowiak, Electrode materials with pseudocapacitive properties, in: Supercapacitors, Wiley-VCH Verlag GmbH & Co. KGaA, Weinheim, Germany, 2013, pp. 207–237.
[3] K. Naoi, Y. Nagano, Li-ion-based hybrid supercapacitors in organic medium, in: Supercapacitors, Wiley-VCH Verlag GmbH & Co. KGaA, Weinheim, Germany, 2013, pp. 239–256.
[4] P. Simon, P.-L. Taberna, F. Béguin, Electrical double-layer capacitors and carbons for EDLCs, in: Supercapacitors, Wiley-VCH Verlag GmbH & Co. KGaA, Weinheim, Germany, 2013, pp. 131–165.
[5] P. Simon, Y. Gogotsi, Nat. Mater 7 (2008) 845–854.
[6] V. Aravindan, J. Gnanaraj, Y.-S. Lee, S. Madhavi, Chem. Rev. 114 (2014) 11619–11635.
[7] J. Yan, Q. Wang, T. Wei, Z. Fan, Adv. Energy Mater. 4 (2014) 1300816.
[8] W.F. Mak, G. Wee, V. Aravindan, N. Gupta, S.G. Mhaisalkar, S. Madhavi, J. Electrochem. Soc. 159 (2012) A1481–A1488.
[9] K. Naoi, S. Ishimoto, J.-I. Miyamoto, W. Naoi, Energy & Environ. Sci. 5 (2012) 9363–9373.
[10] A. Jain, V. Aravindan, S. Jayaraman, P.S. Kumar, R. Balasubramanian, S. Ramakrishna, S. Madhavi, M. Srinivasan, Sci. Rep. 3 (2013). Art 3002.
[11] A. Jain, R. Balasubramanian, M.P. Srinivasan, Chem. Eng. J. 283 (2016) 789–805.
[12] L. Wei, G. Yushin, Nano Energy 1 (2012) 552–565.
[13] I.K. Moon, J. Lee, R.S. Ruoff, H. Lee, Nat. Commun. 1 (2010) 73.
[14] P. Cheng, S. Gao, P. Zang, X. Yang, Y. Bai, H. Xu, Z. Liu, Z. Lei, Carbon 93 (2015) 315–324.
[15] P. Sennu, H.-J. Choi, S.-G. Baek, V. Aravindan, Y.-S. Lee, Carbon 98 (2016) 58–66.
[16] J.-S. Ye, H.F. Cui, X. Liu, T.M. Lim, W.-D. Zhang, F.-S. Sheu, Small 1 (2005) 560–565.
[17] M. Kuang, Z.Q. Wen, X.L. Guo, S.M. Zhang, Y.X. Zhang, J. Power Sources 270 (2014) 426–433.
[18] Z. Tang, C.-H. Tang, H. Gong, Adv. Funct. Mater. 22 (2012) 1272–1278.
[19] J.-K. Chang, C.-M. Wu, I.W. Sun, J. Mater. Chem. 20 (2010) 3729–3735.
[20] C. Xiang, M. Li, M. Zhi, A. Manivannan, N. Wu, J. Power Sources 226 (2013) 65–70.
[21] J. Li, W. Zhao, F. Huang, A. Manivannan, N. Wu, Nanoscale 3 (2011) 5103–5109.
[22] G. Wang, L. Zhang, J. Zhang, Chem. Soc. Rev. 41 (2012) 797–828.
[23] H.-C. Chien, W.-Y. Cheng, Y.-H. Wang, S.-Y. Lu, Adv. Funct. Mater. 22 (2012) 5038–5043.
[24] Z. Wu, Y. Zhu, X. Ji, J. Mater. Chem. A 2 (2014) 14759–14772.
[25] D. Bélanger, T. Brousse, J.W. Long, Electrochem. Soc. Interface 17 (2008) 49–52.
[26] W. Liu, X. Li, M. Zhu, X. He, J. Power Sources 282 (2015) 179–186.
[27] K. Xu, W. Li, Q. Liu, B. Li, X. Liu, L. An, Z. Chen, R. Zou, J. Hu, J. Mater. Chem. A 2 (2014) 4795–4802.
[28] X. Wang, W.S. Liu, X. Lu, P.S. Lee, J. Mater. Chem. 22 (2012) 23114–23119.
[29] X. Wang, A. Sumboja, M. Lin, J. Yan, P.S. Lee, Nanoscale 4 (2012) 7266–7272.
[30] H. Chen, J. Jiang, L. Zhang, D. Xia, Y. Zhao, D. Guo, T. Qi, H. Wan, J. Power Sources 254 (2014) 249–257.
[31] L. Niu, Z. Li, Y. Xu, J. Sun, W. Hong, X. Liu, J. Wang, S. Yang, ACS Appl. Mater. Interfaces 5 (2013) 8044–8052.
[32] N.-S. Choi, Z. Chen, S.A. Freunberger, X. Ji, Y.-K. Sun, K. Amine, G. Yushin, L.F. Nazar, J. Cho, P.G. Bruce, Angew. Chem. Int. Ed. 51 (2012) 9994–10024.
[33] P. Sennu, H.S. Kim, J.Y. An, V. Aravindan, Y.-S. Lee, Chem. – An Asian J. 10 (2015) 1776–1783.
[34] P. Sennu, M. Christy, V. Aravindan, Y.-G. Lee, K.S. Nahm, Y.-S. Lee, Chem. Mater. 27 (2015) 5726–5735.
[35] J.H. Park, O.O. Park, J. Power Sources 111 (2002) 185–190.
[36] E. Frackowiak, F. Béguin, Carbon 39 (2001) 937–950.
[37] A.C. Ferrari, J. Robertson, Phys. Rev. B 61 (2000) 14095–14107.
[38] J. Deng, T. Xiong, F. Xu, M. Li, C. Han, Y. Gong, H. Wang, Y. Wang, Green Chem. 17 (2015) 4053–4060.
[39] J. Wang, L. Shen, P. Nie, X. Yun, Y. Xu, H. Dou, X. Zhang, J. Mater. Chem. A 3 (2015) 2853–2860.
[40] C. Long, X. Chen, L. Jiang, L. Zhi, Z. Fan, Nano Energy 12 (2015) 141–151.
[41] L. Deng, G. Zhang, L. Kang, Z. Lei, C. Liu, Z.-H. Liu, Electrochimica Acta 112 (2013) 448–457.
[42] Z. Li, Z. Xu, H. Wang, J. Ding, B. Zahiri, C.M.B. Holt, X. Tan, D. Mitlin, Energy & Environ. Sci. 7 (2014) 1708–1718.
[43] Y. Yoon, K. Lee, C. Baik, H. Yoo, M. Min, Y. Park, S.M. Lee, H. Lee, Adv. Mater. 25 (2013) 4437–4444.
[44] P. Simon, Y. Gogotsi, Nat. Mater. 7 (2008) 845–854.
[45] A.G. Pandolfo, A.F. Hollenkamp, J. Power Sources 157 (2006) 11–27.
[46] V. Khomenko, E. Raymundo-Pinero, F. Beguin, J. Power Sources 153 (2006) 183–190.
[47] R.R. Salunkhe, J. Lin, V. Malgras, S.X. Dou, J.H. Kim, Y. Yamauchi, Nano Energy 11 (2015) 211–218.
[48] Z. Gu, H. Nan, B. Geng, X. Zhang, J. Mater. Chem. A 3 (2015) 12069–12075.